The Astronomical Journal, 169:288 (10pp), 2025 June https://doi.org/10.3847/1538-3881/adc5e7

Four Planets Found through Microlensing Events Involving Faint Source Stars

Cheongho Han[1], Michael D. Albrow[2], Chung-Uk Lee[3], Sun-Ju Chung[3], Andrew Gould[4,5], Kyu-Ha Hwang[3], Youn Kil Jung[3], Yoon-Hyun Ryu[3], Yossi Shvartzvald[6], In-Gu Shin[7], Jennifer C. Yee[7], Hongjing Yang[8], Weicheng Zang[7,8], Sang-Mok Cha[3,9], Doeon Kim[1], Dong-Jin Kim[3], Seung-Lee Kim[3], Dong-Joo Lee[3], Yongseok Lee[3,9], Byeong-Gon Park[3], and Richard W. Pogge[5]

[1] Department of Physics, Chungbuk National University, Cheongju 28644, Republic of Korea; cheongho@astroph.chungbuk.ac.kr
[2] University of Canterbury, Department of Physics and Astronomy, Private Bag 4800, Christchurch 8020, New Zealand
[3] Korea Astronomy and Space Science Institute, Daejon 34055, Republic of Korea; leecu@kasi.re.kr
[4] Max Planck Institute for Astronomy, Königstuhl 17, D-69117 Heidelberg, Germany
[5] Department of Astronomy, The Ohio State University, 140 W. 18th Ave., Columbus, OH 43210, USA
[6] Department of Particle Physics and Astrophysics, Weizmann Institute of Science, Rehovot 76100, Israel
[7] Center for Astrophysics, Harvard & Smithsonian, 60 Garden St., Cambridge, MA 02138, USA
[8] Department of Astronomy and Tsinghua Centre for Astrophysics, Tsinghua University, Beijing 100084, People's Republic of China
[9] School of Space Research, Kyung Hee University, Yongin, Kyeonggi 17104, Republic of Korea

Received 2024 October 23; revised 2025 February 27; accepted 2025 March 24; published 2025 May 2

Abstract

To conduct a comprehensive demographic study of microlensing planets, it is essential to detect all planetary signals that exceed a predefined threshold through a detailed analysis of survey data. We reanalyzed previous data from the Korea Microlensing Telescope Network survey to search for weak planetary signals in lensing events involving faint source stars. For events with potential short-term anomalies identified in the initial search, we validated the signals using rereduced data and conducted detailed modeling of the anomalous events. This process led to the discovery of four planetary events: KMT-2017-BLG-2197, KMT-2022-BLG-1790, KMT-2022-BLG-2076, and KMT-2023-BLG-2209. For all these events, the modeling resulted in two solutions due to the well-known inner–outer degeneracy. The estimated masses of the planets and their hosts are approximately $(M_{\rm p}/M_{\rm J}, M_{\rm h}/M_\odot) \sim (0.36, 7.9)$ for KMT-2017-BLG-2197L, $\sim(0.6, 1.7)$ for KMT-2022-BLG-1790L, $\sim(0.67, 0.9)$ for KMT-2022-BLG-2076L, and $\sim(0.73, 0.8)$ for KMT-2023-BLG-2209L. The planetary systems KMT-2017-BLG-2197L and KMT-2022-BLG-1790L are likely located in the Galactic bulge, while KMT-2022-BLG-2076L and KMT-2023-BLG-2209L are more likely situated in the disk.

Unified Astronomy Thesaurus concepts: Gravitational microlensing exoplanet detection (2147); Gravitational microlensing (672)

Materials only available in the online version of record: data behind figures

1. Introduction

Since 2015, the Korea Microlensing Telescope Network (KMTNet) group has been conducting a microlensing experiment focused on detecting extrasolar planets. This is accomplished by high-cadence monitoring of stars in the Galactic bulge using three telescopes strategically positioned on three continents in the Southern Hemisphere (S.-L. Kim et al. 2016). The experiment has detected over 3000 microlensing events annually, with about 1% of these events indicating planetary signals. The microlensing technique is particularly suited for detecting cold planets located beyond the snow line in planetary systems, which are challenging to detect through other methods. As a result, the planetary sample collected from this experiment will provide an essential foundation for demographic studies of exoplanets.

For a comprehensive demographic study of microlensing planets, it is essential to detect all planetary signals that exceed a predefined threshold through detailed analysis of the survey data. However, several challenges complicate the detection process. One challenge arises when the signal is only partially captured, leading to degeneracies in the analysis that obscure accurate determination of lensing parameters or suggest nonplanetary interpretations. Additionally, planetary signals may deviate from their typical form, often due to the presence of a binary companion to the planet's host star or an additional planetary body in the system. A binary companion to the source star can similarly distort the planetary signal. Signal strength also poses a difficulty; strong signals generally occur when the source crosses caustics induced by planets, but signals without caustic crossings are usually weaker. Moreover, planetary signals in events involving faint source stars can be particularly challenging to identify, as they may be obscured by a background of large error bars.

Systematic analyses of KMTNet data have been conducted to detect planetary signals that are challenging to identify. C. Han et al. (2023b) reported the discovery of three planets—KMT-2021-BLG-2010Lb, KMT-2022-BLG-0371Lb, and KMT-2022-BLG-1013Lb—based on partially covered signals. In an extended investigation of the 2023 KMTNet data, C. Han et al. (2024b) identified three additional planets—KMT-2021-BLG-2010Lb, KMT-2022-BLG-0371Lb, and KMT-2022-BLG-1013Lb—also from partially covered signals. C. Han et al. (2022a) discovered the planetary system KMT-2021-BLG-1077L, hosting two giant planets, through a systematic analysis of signals deviating from the standard form. Additionally, C. Han et al. (2024a) found that the planetary signal of OGLE-2023-BLG-0836Lb was

Table 1
Source Coordinates, *I*-band Extinction, Observation Field, and Cadence

Event	(R.A., Decl.)$_{\mathrm{J2000}}$	(l, b)	I_{base}	A_I	Field	Cadence (hr)
KMT-2017-BLG-2197	(17:30:26.72, −30:09:33.52)	$(-2\overset{\circ}{.}7996, 2\overset{\circ}{.}1336)$	19.91	2.67	BLG11	2.5
KMT-2022-BLG-1790	(18:04:13.50, −27:02:05.10)	$(3\overset{\circ}{.}7159, -2\overset{\circ}{.}5851)$	20.41	1.24	BLG03, BLG43	0.25
KMT-2022-BLG-2076	(17:52:12.27, −29:01:40.55)	$(0\overset{\circ}{.}6632, -1\overset{\circ}{.}2815)$	20.57	2.91	BLG42	0.5
KMT-2023-BLG-2209	(17:55:58.61, −29:18:20.41)	$(0\overset{\circ}{.}8402, -2\overset{\circ}{.}1324)$	19.02	1.94	BLG02, BLG42	0.25

distorted by the presence of a binary companion to the planet's host star. C. Han et al. (2022b) identified the binary-source origin of deformed planetary signals in the events KMT-2021-BLG-1547 and KMT-2021-BLG-1898. In the case of KMT-2021-BLG-0240, signal deformation was attributed to either an additional planet or a binary companion to the source (C. Han et al. 2022c). C. Han et al. (2023a) reported the discovery of two planets—KMT-2022-BLG-0475Lb and KMT-2022-BLG-1480Lb—detected through weak signals from a non-caustic-crossing channel. Furthermore, C. Han et al. (2021) identified three microlensing planets—KMT-2017-BLG-2509Lb, OGLE-2017-BLG-1099Lb, and OGLE-2019-BLG-0299Lb—through systematic searches for weak planetary signals in the light curves of events with faint source stars.

Most planet-induced anomalies in KMTNet microlensing events are detected using the semiautomatic AnomalyFinder algorithm (W. Zang et al. 2021). Traditional methods identify anomalies by detecting local χ^2 excesses within a specified time range. However, these approaches often fail to account for correlated residuals, which can lead to false positives due to systematic effects in the data. The KMTNet AnomalyFinder improves detection accuracy through additional refinement procedures. First, anomalies that pass the initial threshold (as in the classical method) are further analyzed by fitting them with a PSPL model[10] and evaluating them against a second threshold, effectively filtering out most false signals caused by systematics. Second, low-threshold candidate anomalies with small signal-to-noise ratios undergo individual visual inspection to verify their authenticity. In this procedure, auxiliary information, such as seeing and sky background, is used to eliminate bad points that frequently generate false signals. The effectiveness of the AnomalyFinder algorithm was demonstrated through its application to the known 2019 KMTNet planetary events, where it successfully identified signals in all cases. Microlensing planets identified during the 2015–2019 period with the use of the AnomalyFinder algorithm were published in a series of papers: W. Zang et al. (2021), K.-H. Hwang et al. (2022), H. Wang et al. (2022), A. Gould et al. (2022), W. Zang et al. (2022), Y. K. Jung et al. (2022), W. Zang et al. (2023), Y. K. Jung et al. (2023), I.-G. Shin et al. (2023), Y.-H. Ryu et al. (2024), I.-G. Shin et al. (2024), and Y. Gui et al. (2024).

In this work, we report the discovery of four microlensing planets identified through an extended investigation of lensing events involving faint source stars. These planets are KMT-2017-BLG-2197Lb, KMT-2022-BLG-1790Lb, KMT-2022-BLG-2076Lb, and KMT-2023-BLG-2209Lb. Documenting these planetary events with weak signals is important not only for constructing a complete planet sample but also for assessing the overall performance of the AnomalyFinder algorithm and accounting for this in future statistical analyses.

2. Observations and Data

All the planets reported in this work were discovered through the analysis of events exclusively detected by the KMTNet survey. The KMTNet survey operates using three telescopes located at Siding Spring Observatory in Australia (KMTA), Cerro Tololo Inter-American Observatory in Chile (KMTC), and South African Astronomical Observatory in South Africa (KMTS). These identical telescopes each feature a 1.6 m aperture and are equipped with a camera offering a 4 deg^2 field of view. The events were identified using the KMT EventFinder system (D.-J. Kim et al. 2018) applied to the data. Table 1 lists the event ID, equatorial coordinates (R.A., decl.)$_{\mathrm{J2000}}$, Galactic coordinates (l, b), *I*-band baseline magnitude (I_{base}), extinction toward the field (A_I), KMTNet field name, and observational cadence. For the events KMT-2022-BLG-1790 and KMT-2023-BLG-2209, the source is located in the overlapping region of two primary fields, toward which observations were conducted with a 0.5 hr cadence for each field, resulting in a combined cadence of 0.25 hr.

Observations of the events were primarily carried out in the *I* band of the Johnson–Cousins *BVRI* filter system. To determine the source color of the events, approximately one-tenth of the images were taken in the *V* band. The observational cadence varied from 0.25 to 2.5 hr, depending on the event. Photometry of the online data was performed using the KMTNet pySIS pipeline (M. Albrow et al. 2009). For optimal results, the photometric data used in the analysis were derived from a rereduction of the images with the code developed by H. Yang et al. (2024). For a subset of KMTC data, additional photometry was performed using the pyDIA code (M. Albrow 2017) to create light curves in the *V* and *I* bands, as well as color–magnitude diagrams (CMDs) of stars near the source.

For the data used in the analysis, we adjusted the errors to ensure that they aligned with the scatter of the data and that the χ^2 value for the best-fit model equaled unity for each data set. This rescaling of error bars was carried out using the method described in J. C. Yee et al. (2012). Errors estimated by photometric packages are typically smaller than the true errors, which also include contributions from systematics. Consequently, the uncertainties in lensing parameters derived from modeling with adjusted error bars are generally larger than those obtained from the data before the adjustment. However, it is important to note that since the error bars are fine tuned, the variation in the lensing parameters remains minimal.

3. Analysis

In microlensing, a planet usually reveals its presence as a brief, discontinuous signal superimposed on the lensing light

---

[10] Planet-induced signals manifest not only as bumps but also as dips and U-shaped caustic-crossing features. However, dips can be considered the inverse of bumps, while U-shaped features as a whole can be treated as bumps.

curve generated by the host star (S. Mao & B. Paczyński 1991; A. Gould & L. Loeb 1992). This signal occurs when the source approaches the region near caustics produced by the planet. Caustics represent the locations in the source plane at which the magnification of a point source becomes infinite. A planetary companion to the lens induces two types of caustics: "central" and "peripheral" caustics.[11] The central caustic appears near the position of the planet's host star, while the peripheral caustic occurs farther away, at the position $\boldsymbol{s} - 1/\boldsymbol{s}$, where $\boldsymbol{s}$ represents the position vector of the planet relative to the host, with its length scaled to the angular Einstein radius (θe). The properties of planet-induced caustics are discussed in detail by S.-J. Chung et al. (2005) for central caustics and by C. Han (2006) for peripheral caustics. The light curves of the analyzed lensing events exhibited a short-term anomaly, characteristic of typical planetary events.

We analyzed the properties of the planet causing the observed anomalies by modeling the lensing light curve to determine the lensing parameters that best explain the anomaly. For a lensing event involving a binary lens system and a single source (a 2L1S event), the light curve is characterized by seven basic parameters. The first two parameters, t_0 and u_0, describe the lens–source approach, where t_0 is the time of closest lens–source approach and u_0 represents the separation (scaled to θe) at that time. Another parameter, $t_{\rm E}$, defines the event timescale as the time needed for the source to cross θe. In a lensing event involving a single-mass lens and a single source star (a 1L1S event), the light curve is defined by these three parameters. The binary lens system is described by two additional parameters: s, the projected separation (scaled to θe), and q, the mass ratio of the lens components. The parameter α, which is the angle between the source's proper motion vector μ and the binary lens axis, specifies the direction of the source's motion. Lastly, the parameter ρ, the ratio of the angular source radius θ_* to the angular Einstein radius θe, describes the finite-source lensing magnifications during caustic crossings.

The modeling was conducted in two stages. In the first stage, a grid search was performed to determine the parameters (s, q) of the binary lens. During this stage, the source incidence angle α was assigned initial values uniformly distributed over the interval $0 < \alpha \leqslant 2\pi$ with multiple divisions, while the remaining parameters were estimated using a downhill approach based on the Markov Chain Monte Carlo method. In the second stage, after identifying local solutions using the χ^2 map in the (s, q) plane from the first stage, each local solution was further refined by allowing all parameters to vary freely. We assessed degeneracy among different solutions by comparing the χ^2 values of each local solution. For events with multiple degenerate solutions, we present all of these solutions and explore the underlying causes of the degeneracy. In the following subsections, we provide analyses for each individual event.

3.1. KMT-2017-BLG-2197

The lensing event KMT-2017-BLG-2197 occurred early in the bulge season and reached its peak on 2017 April 13, corresponding to the abridged Heliocentric Julian date $\mathrm{HJD}' \equiv \mathrm{HJD} - 2450000 = 7857$. The light curve of the event, shown in Figure 1, reveals a short-term anomaly lasting about half a day, occurring near the peak with a moderately high magnification of $A_{\rm max} \sim 17$. The anomaly was covered by six data points, including two from KMTS observations and four from KMTC observations. The U-shaped variation observed in the central region suggests that the anomaly was likely caused by the source crossing a small caustic induced by a companion to the lens. The anomaly was initially hard to detect in the online data processed by the automated pipeline, as it was masked by outliers. However, the rereduction of the data, performed to verify the anomaly's authenticity, clearly revealed the anomalous nature of the signal.

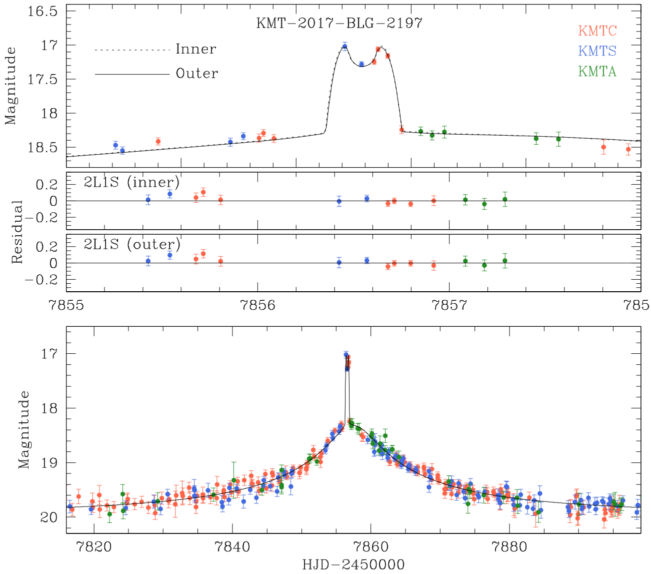

Figure 1. Light curve of the lensing event KMT-2017-BLG-2197. The bottom panel shows the overall view, while the top presents a zoomed-in view around the anomaly. The curves overlaid on the data points represent the inner and outer 2L1S solutions, while the two lower panels display the residuals from these models. The colors of the data points correspond to the telescopes indicated in the legend.

(The data used to create this figure are available in the online article.)

Modeling the light curve revealed two sets of 2L1S solutions. The binary parameters for one solution, referred to as the "inner solution," are $(s, q)_{\rm in} \sim (1.54, 2.4 \times 10^{-2})$, while the parameters for the other solution, called the "outer solution," are $(s, q)_{\rm out} \sim (0.72, 1.9 \times 10^{-2})$. The terms "inner" and "outer" solutions are designated for reasons explained below. Table 2 provides the full lensing parameters for both solutions. The degeneracy between the solutions is significant, with a χ^2 difference of only $\Delta\chi^2 = 0.2$. The model curves for both solutions are shown in Figure 1, though they are nearly indistinguishable within the thickness of the line.

Figure 2 displays the lens-system configurations corresponding to the inner and outer solutions. In both scenarios, the anomaly was generated by the source passing through the central caustic induced by a low-mass companion to the lens. For the inner solution, the source passed through the inner region between the central and peripheral caustics, whereas in the outer solution, it moved through the outer region of the caustic. This distinction is why the solutions are termed "inner" and "outer." The four KMTC data points resolve the caustic when the source exited the caustic, and this allows us to measure the normalized source radius of $\rho \sim 2.5 \times 10^{-3}$.

---

[11] The peripheral caustic is often referred to as the "planetary caustic," even though the central caustic is also produced by a planet. To ensure consistent naming based on their locations, we use the term "peripheral caustic" to designate the caustic located farther from the host star.

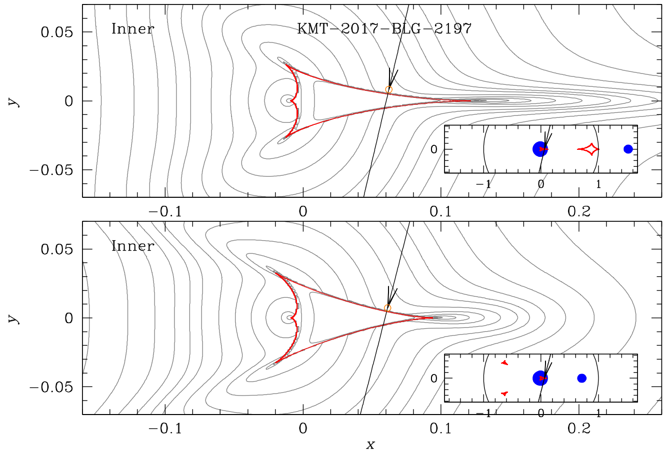

Figure 2. Lens-system configuration of KMT-2017-BLG-2197 for the inner solution (upper panel) and outer solution (lower panel). In each panel, the cuspy figure represents the caustic, the arrowed line indicates the source trajectory, and the curves surrounding the caustic depict the equimagnification contours. The inset offers a zoomed-out view of the configuration, showing the two blue dots as the positions of the lens components and a circle of unit radius representing the Einstein ring. Lengths are scaled to the Einstein radius of the lens, and the coordinates are centered at the position of the planet's host star.

Table 2
Lensing Parameters of KMT-2017-BLG-2197

Parameter	Inner	Outer
χ^2	665.8	666.0
t_0 (HJD′)	7857.177 ± 0.053	7857.221 ± 0.063
u_0 (10^{-2})	6.06 ± 0.77	5.76 ± 0.66
t_E (days)	42.40 ± 4.57	44.00 ± 4.10
s	1.540 ± 0.041	0.723 ± 0.017
q (10^{-2})	2.36 ± 0.35	1.85 ± 0.29
α (rad)	4.947 ± 0.021	4.963 ± 0.025
ρ (10^{-3})	2.52 ± 0.35	2.33 ± 0.3

Note. HJD′ = HJD − 2450000.

The similarity between the model curves of the two solutions results from the "inner–outer" degeneracy. Initially proposed to describe the similarity between light curves produced by source passages through the inner and outer regions of the peripheral caustic (B. S. Gaudi & A. Gould 1997), this degeneracy was later found to be broadly applicable to perturbations involving central caustics (A. Herrera-Martin et al. 2020; J. C. Yee et al. 2021; K.-H. Hwang et al. 2022; K. Zhang et al. 2022). A. Gould et al. (2022) demonstrated that the lensing parameters of solutions with this degeneracy follow the relation

$$\sqrt{s_{\rm in} \times s_{\rm out}} = s^{\dagger}_{\pm}; \qquad s^{\dagger}_{\pm} = \frac{\sqrt{u_{\rm anom} + 4} \pm u_{\rm anom}}{2}, \tag{1}$$

where $s_{\rm in}$ and $s_{\rm out}$ denote the binary separations of the inner and outer solutions, respectively, $u_{\rm anom} = (u_0^2 + \tau_{\rm anom}^2)^{1/2}$, $\tau_{\rm anom} = (t_{\rm anom} - t_0)/t_E$, and $t_{\rm anom}$ indicates the time of the anomaly. In the equation on the right, the sign is "+" for anomalies with a bump feature and "−" for those with a dip feature. Since the observed anomaly displays a bump, the sign is "+." From the lensing parameters provided in Table 1, we find the geometric mean of the binary separations $\sqrt{s_{\rm in} \times s_{\rm out}} = 1.06$ matches well the value of $s^{\dagger}_{+} = 1.03$.

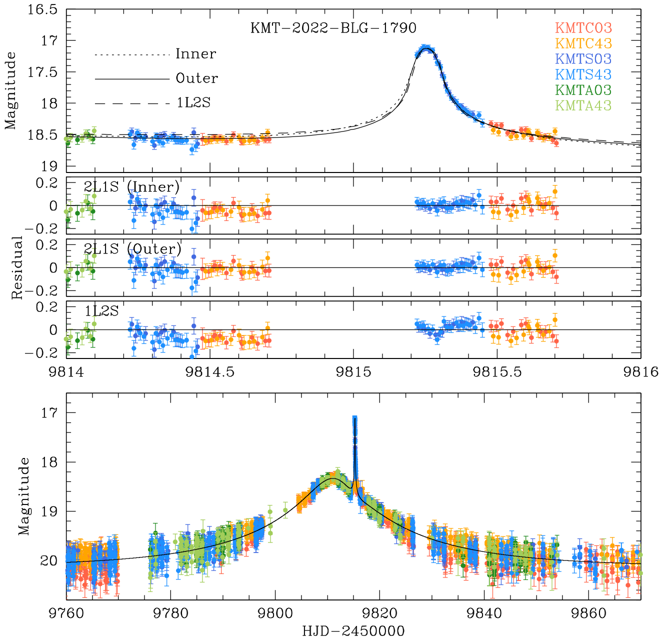

Figure 3. Lensing light curve of KMT-2022-BLG-1790.
(The data used to create this figure are available in the online article.)

3.2. KMT-2022-BLG-1790

The lensing event KMT-2022-BLG-1790 also occurred on a faint source star, reaching a maximum magnification of $A_{\rm max} \sim 6.9$ on 2022 August 19, corresponding to HJD′ = 9811. The event was detected 3 days before its peak using the EventFinder system, which has been fully operational since the 2018 season. The event timescale, determined from 1L1S modeling by excluding the data around the anomaly, is approximately $t_E \sim 34$ days.

Figure 3 shows the light curve of the event constructed from the reprocessed data. It revealed a distinct anomaly that occurred 4 days after the peak, with a maximum deviation of $\Delta I \sim 1.7$ mag from the underlying 1L1S model. The anomaly featured a single peak, with the top and falling side resolved by the combined KMTS and KMTC data sets. The rising part of the anomaly occurred during nighttime at the Australian site, but no data could be acquired because of unfavorable sky conditions.

We evaluated two modeling approaches to interpret the observed anomaly, given that a single-peak short-term anomaly can be attributed to either a companion to the lens (2L1S interpretation) or a companion to the source (1L2S interpretation), as noted by B. S. Gaudi (1998), B. S. Gaudi & C. Han (2004), and K.-H. Hwang et al. (2013). Our analysis strongly rejected the binary-source origin of the anomaly, with a confidence level of $\Delta\chi^2 = 161.4$. Under the 2L1S interpretation, we identified a pair of solutions due to inner–outer degeneracy. The lensing parameters for both the inner and outer 2L1S solutions are listed in Table 3. Figure 3 presents the model curves for the 2L1S solutions along with the 1L2S model for comparison. For both 2L1S solutions, the estimated mass ratios are very low—$q \sim 3.5 \times 10^{-3}$ for the inner solution and $q \sim 2.8 \times 10^{-3}$ for the outer solution—indicating that the lens companion is likely a planet-mass object. Comparing the two 2L1S solutions showed that the outer solution provided a significantly better fit to the data, with

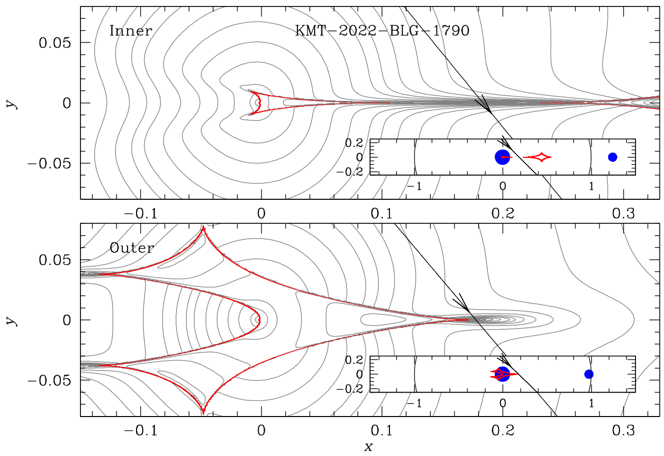

Figure 4. Lens-system configuration of KMT-2022-BLG-1790.

Table 3
Lensing Parameters of KMT-2022-BLG-1790

Parameter	Inner	Outer
χ^2	5760.3	5716.4
t_0 (HJD$'$)	9811.313 ± 0.029	9811.300 ± 0.028
u_0 (10^{-2})	1.1421 ± 0.0042	0.1359 ± 0.0064
t_E (days)	33.91 ± 0.74	34.51 ± 1.27
s	1.2434 ± 0.0039	0.9755 ± 0.0070
q (10^{-3})	3.456 ± 0.17	2.844 ± 0.14
α (rad)	4.0269 ± 0.0057	4.0116 ± 0.0071
ρ (10^{-3})	1.35 ± 0.12	1.38 ± 0.12

$\Delta\chi^2 = 43.9$. Consequently, the subsequent analysis is based on the outer solution.

Figure 4 illustrates the lens-system configurations for both the inner and outer solutions. In the outer solution, the lens generates a single resonant caustic with six folds, and the anomaly occurs as the source passes through the region just in front of the strong on-axis cusp. In contrast, the inner solution features a caustic composed of two segments, with distinct central and peripheral caustics. The anomaly arises when the source traverses the region of positive deviation between the on-axis cusps of these caustics. With the dense coverage of the anomaly near the peak and the descending side, the normalized source radius was precisely measured as $\rho = (1.38 \pm 0.12) \times 10^{-3}$.

3.3. KMT-2022-BLG-2076

The lensing event KMT-2022-BLG-2076 occurred on a faint source, which had a baseline magnitude of $I \sim 20.6$. It reached its maximum magnification of $A_{\rm max} \sim 90$ on 2022 September 2 (HJD$' = 9825$), and the event was identified 2 days after this peak. An anomaly occurred half a day before the peak, but it was not noticed during the initial inspection of the data processed using the automated pipeline. However, a subsequent review of the online data suggested a likely anomaly, which was clearly identified in the light curve after reprocessing the data. The anomaly lasted for about half a day, and the timescale, determined from a 1L1S model excluding the data around the anomaly, is approximately 35 days.

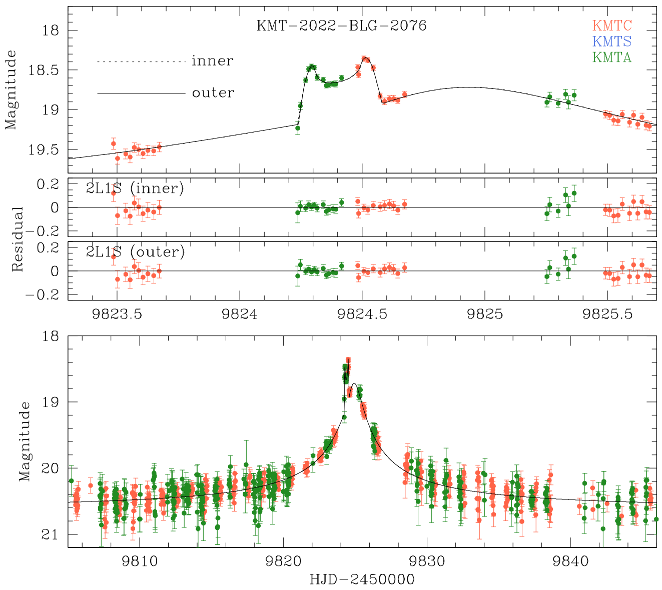

Figure 5. Light curve of the lensing event KMT-2022-BLG-2076. (The data used to create this figure are available in the online article.)

Table 4
Lensing Parameters of KMT-2022-BLG-2076

Parameter	Inner	Outer
χ^2	2373.3	2374.0
t_0 (HJD$'$)	9824.863 ± 0.012	9824.863 ± 0.012
u_0 (10^{-2})	0.0146 ± 0.0014	0.0146 ± 0.0016
t_E (days)	35.28 ± 3.14	35.25 ± 3.82
s	1.1423 ± 0.0078	0.8946 ± 0.0065
q (10^{-3})	1.25 ± 0.14	1.22 ± 0.15
α (rad)	5.448 ± 0.022	5.453 ± 0.019
ρ (10^{-3})	0.808 ± 0.083	0.796 ± 0.095

Figure 5 displays the light curve of KMT-2022-BLG-2076, including a close-up view of the anomaly. The profile of the anomaly clearly shows that it resulted from the source crossing over a caustic. The rising part of the anomaly was captured by the KMTA data, while the falling part was recorded by the KMTC data, with the U-shaped trough covered by both data sets. Given its brief duration and position in the light curve, the caustic responsible for the anomaly is likely a small central caustic generated by a low-mass companion.

Detailed modeling of the light curve confirmed that the anomaly is of planetary origin. We identified two sets of solutions with binary parameters: $(s, q)_{\rm in} \sim (1.14, 1.25 \times 10^{-3})$ for one solution and $(s, q)_{\rm out} \sim (0.89, 1.22 \times 10^{-3})$ for the other. The model curves for these solutions are shown in Figure 5, and the full lensing parameters are listed in Table 4. The solutions are highly degenerate, with $\Delta\chi^2 = 0.7$. The close match between $s^\dagger = 1.010$ and the geometric mean $\sqrt{s_{\rm in} \times s_{\rm out}} = 1.010$ suggests that the similarity between the models is caused by the inner–outer degeneracy. Apart from the binary separation, the other parameters of the two solutions are very similar to each other.

The upper and lower panels of Figure 6 illustrate the lens-system configurations for the inner and outer solutions. In the inner solution, the central and peripheral caustics are connected by a narrow bridge, while in the outer solution, the two sets of caustics are separated. In both cases, the source passed through the central caustic at an angle before its closest approach to the planet's host star. Based on the clear profile of the anomaly, the normalized source size was well constrained at $\rho \sim 0.8 \times 10^{-3}$.

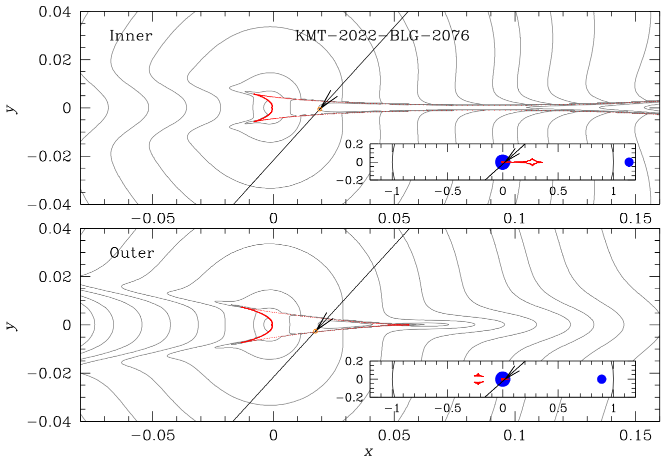

Figure 6. Lens-system configuration of KMT-2023-BLG-2076.

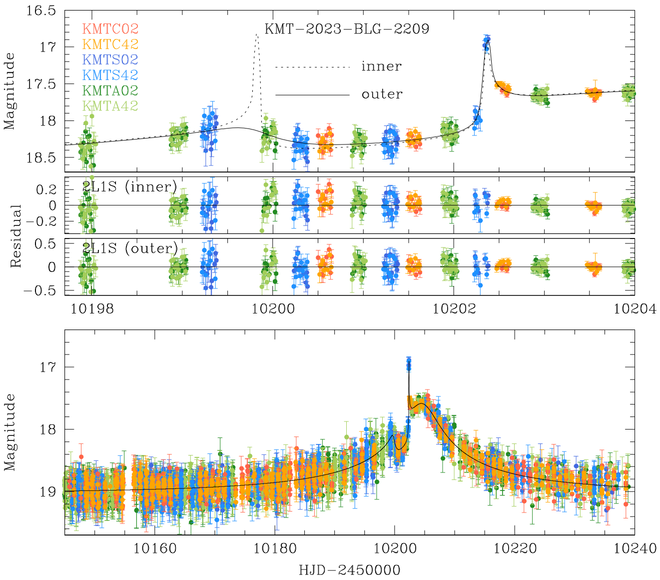

Figure 7. Lensing light curve of KMT-2023-BLG-2209.
(The data used to create this figure are available in the online article.)

3.4. KMT-2023-BLG-2209

The lensing event KMT-2023-BLG-2209 occurred on a source with an I-band baseline magnitude of $I_{\rm base} = 19.02$. It was detected on 2023 September 14 (HJD$' = 10202$), approximately 2 days before reaching a moderately high peak magnification of $A_{\rm max} \sim 18.5$. At the time of discovery, an anomaly was already in progress, lasting for about 2.5 days during the period $10199 \lesssim {\rm HJD}' \lesssim 10203$. The anomaly in the data processed by the automated pipeline was initially detected from a distinct peak around HJD$' \sim 10202.3$. However, upon examining the light curve from the reprocessed data, additional negative deviations from the underlying 1L1S model were found before the peak.

The light curve of KMT-2023-BLG-2209 is shown in Figure 7. The anomaly is characterized by a region of negative deviation during $10199 \lesssim {\rm HJD}' \lesssim 10203$ and a strong peak at HJD$' \sim 10202.3$. The profile of the anomaly differs from the typical pattern seen in caustic crossings, not only because the peak expected from the caustic entrance was absent, but also because the negative deviation does not follow the usual U-shaped pattern. Although the event occurred within the primary fields KMT02 and KMT42, toward which observations were conducted with a 15 minute cadence, there are gaps in the data from different observatories because of the short duration of nighttime at the late stage of the bulge season.

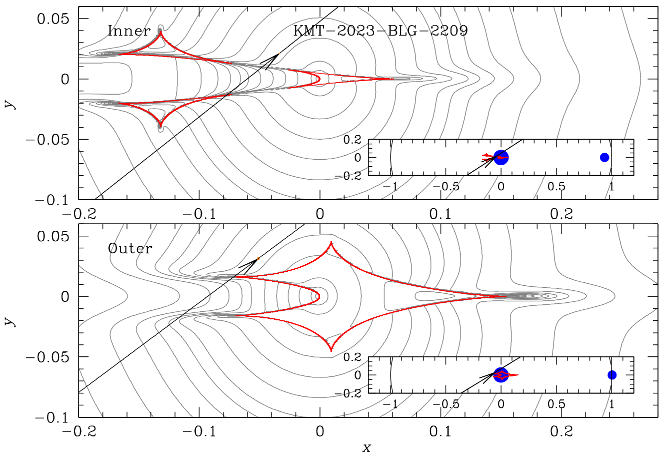

Figure 8. Lens-system configuration of KMT-2023-BLG-2209.

Table 5
Lensing Parameters of KMT-2023-BLG-2209

Parameter	Inner	Outer
χ^2	4938.4	4858.1
t_0 (HJD$'$)	10204.452 ± 0.023	10204.541 ± 0.025
u_0 (10^{-2})	0.0374 ± 0.0017	0.0557 ± 0.0035
$t_{\rm E}$ (days)	67.01 ± 2.64	45.67 ± 2.45
s	0.9361 ± 0.0012	1.0044 ± 0.0031
q (10^{-3})	0.631 ± 0.027	1.046 ± 0.068
α (rad)	2.4729 ± 0.0069	2.5017 ± 0.0075
ρ (10^{-3})	0.3098 ± 0.0561	0.82 ± 0.15

Detailed modeling under a 2L1S interpretation revealed that the anomaly was generated by a planetary companion to the lens. We identified two sets of solutions with binary parameters: $(s,\, q)_{\rm in} \sim (0.94,\ 0.63 \times 10^{-3})$ for one set and $(s,\, q)_{\rm out} \sim (1.00,\ 1.05 \times 10^{-3})$ for the other. The close match between $s_{+}^{\dagger} = 0.958$ and $\sqrt{s_{\rm in} \times s_{\rm out}} = 0.968$ indicates that the similarity between the two models is caused by the inner–outer degeneracy. Table 5 provides the complete lensing parameters for both solutions, together with the χ^2 values of the fits. The model curves and residuals of both solutions are presented in Figure 7. By comparing the fits of the two solutions, it is found that the outer solution offers a significantly better fit compared to the inner solution, with a $\Delta\chi^2 = 80.3$. Therefore, we will proceed with the subsequent analysis based on the outer solution.

The configuration of the lens system for KMT-2023-BLG-2209 is depicted in Figure 8. In the outer solution, which provides a better fit, the caustic induced by the planet has a resonant form with six folds. The extended negative deviation was caused by the source passing through the backend region of the caustic, while the subsequent peak was produced by the source crossing the tip of the upper left cusp. In the inner solution, both the central and peripheral caustics are detected, with the source approaching the caustic cusp twice: initially when it crossed the tip of the lower peripheral caustic, and later as it neared a cusp of the central caustic. This resulted in two peaks, with the earlier peak occurring in a region not covered by the data. The normalized source radius,

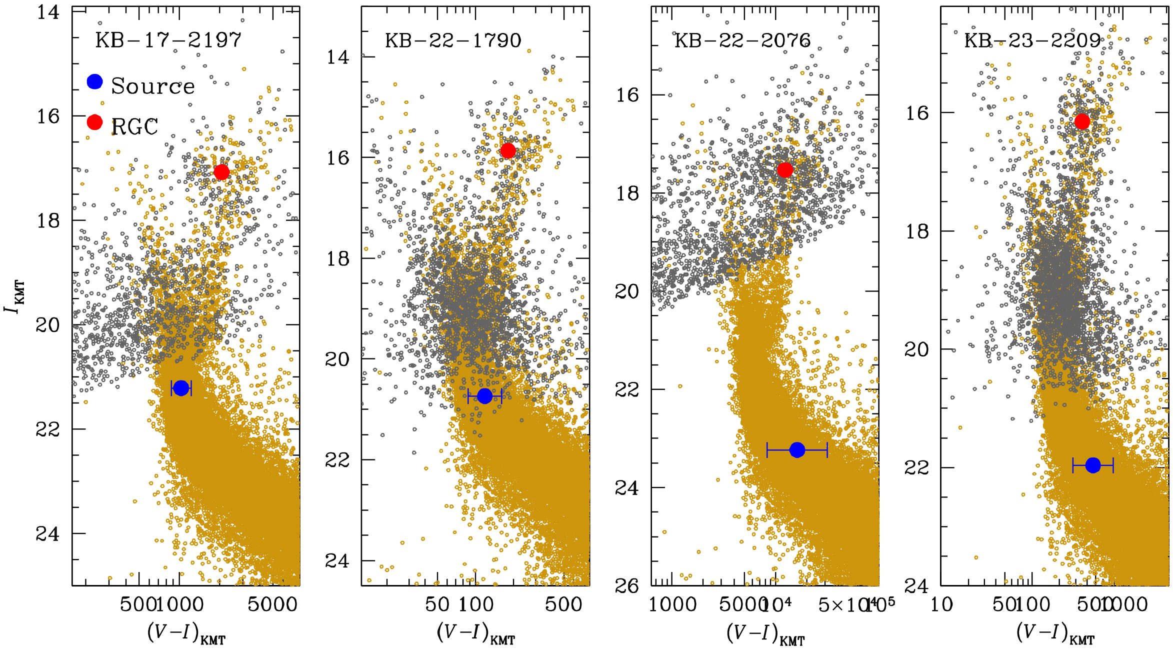

Figure 9. Positions of source stars with respect to the centroids of red giant clumps (RGC) in the color–magnitude diagrams constructed by combining the KMTC (gray dots) and HST (brown dots) observations.

Table 6
Source Parameters, Angular Einstein Radius, and Relative Lens–Source Proper Motion

Quantity	KB-17-2197	KB-22-1790	KB-22-2076	KB-23-2209
$(V-I)$	3.016 ± 0.073	2.074 ± 0.133	4.210 ± 0.290	2.671 ± 0.221
I	21.214 ± 0.010	20.737 ± 0.023	23.237 ± 0.103	21.964 ± 0.097
$(V-I, I)_{\rm RGC}$	(3.319, 17.076)	(2.258, 15.866)	(4.094, 17.533)	(2.553, 16.149)
$(V-I, I)_{\rm RGC,0}$	(1.060, 14.582)	(1.060, 14.335)	(1.060, 14.412)	(1.060, 14.404)
$(V-I)_0$	0.757 ± 0.073	0.876 ± 0.133	1.176 ± 0.290	1.178 ± 0.221
I_s	18.721 ± 0.010	19.206 ± 0.023	20.116 ± 0.103	20.218 ± 0.097
Type	G6V	K1V	K4V	K4V
θ_* (μas)	0.598 ± 0.061	0.546 ± 0.082	0.507 ± 0.151	0.485 ± 0.112
$\theta_{\rm E}$ (mas)	0.237 ± 0.041	0.396 ± 0.069	0.627 ± 0.198	0.720 ± 0.235
μ (mas yr^{-1})	2.045 ± 0.415	4.186 ± 0.744	6.494 ± 2.126	5.602 ± 1.876

$\rho = (0.82 \pm 0.15) \times 10^{-3}$, was measured from the data covering the peak, which were influenced by finite-source effects.

4. Source Stars and Angular Einstein Radii

In this section, we characterize the source stars of the events. By characterizing the source star, one can obtain its angular radius θ_*, which, combined with the measured normalized source radius, allows us to estimate the angular Einstein radius using the relation

$$\theta_{\rm E} = \frac{\theta_*}{\rho}. \tag{2}$$

The source is characterized by measuring its color and magnitude. For events with well-constructed I- and V-band light curves, the source flux (F_s) is determined by fitting the observed light curve ($F_{\rm obs}$) to the lens model [$A(t)$] using the relation

$$F_{\rm obs} = A(t) F_s + F_b, \tag{3}$$

where F_b represents the flux from blended stars. However, for all analyzed events, the V-band photometry was insufficient to accurately measure the V-band flux of the source star, making it challenging to estimate the source color in the usual way.

To characterize the source using only the measured I-band light curve, we applied a method that utilizes the Hubble Space Telescope (HST) CMD constructed from observations of stars in Baade's window by J. A. Holtzman et al. (1998). In the first step, we aligned the CMD from the pyDIA photometry (M. Albrow 2017) of the KMTC data with the HST CMD by matching the centroids of the red giant clumps (RGCs) in both diagrams. The source color was then estimated as the median color of stars on the giant or main-sequence branches, within the measured I-band magnitude difference from the RGC centroid. Figure 9 displays the positions of the source stars in the combined CMDs. Table 6 provides the instrumental colors and magnitudes, $(V-I, I)$, of the source stars, together with those of the RGC centroids, $(V-I, I)_{\rm RGC}$. We calibrated the source color and magnitude using the J. Yoo et al. (2004) method, which references the RGC centroid for calibration because of its well-established values from previous studies (T. Bensby et al. 2013; D. M. Nataf et al. 2013). The calibrated source color and magnitude, $(V-I, I)_0$, are listed in Table 6, along with the spectral types of the source stars. The source

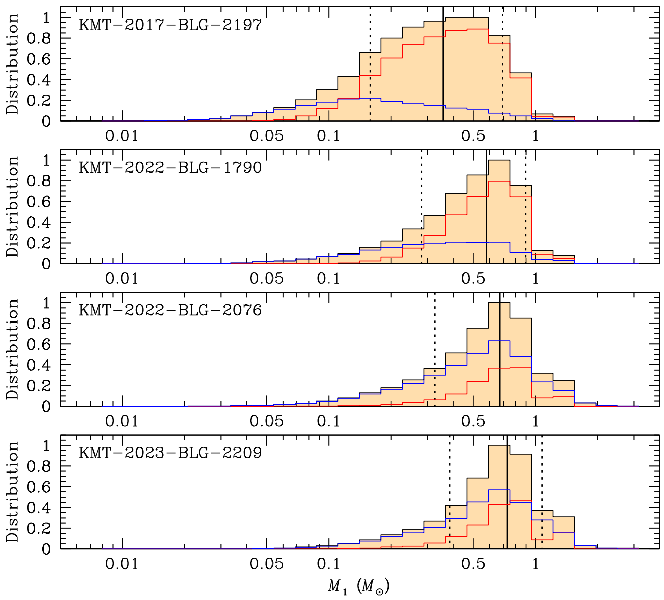

Figure 10. Bayesian posteriors of the host masses of the planetary systems. In each panel, the distributions shown in blue and red curves represent the contributions from disk and bulge lens populations, respectively, while the black curve denotes the combined contribution from both populations. The solid vertical line marks the median of the distribution, and the dotted vertical lines represent the 1σ uncertainty range.

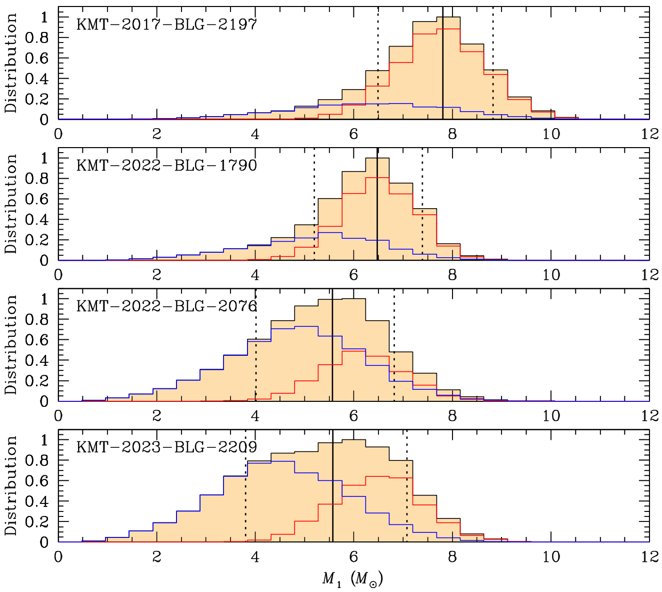

Figure 11. Bayesian posteriors of the distances to the planetary systems. The notations are the same as those in Figure 10.

stars are found to be faint main-sequence stars with spectral types ranging from late G type to early K type.

The angular source radius is estimated using the dereddened color and magnitude. We applied the relation between ($V - K$, V) and θ_* established by P. Kervella et al. (2004). To use this relation, we first converted $V - I$ to $V - K$ using the color–color relation from M. S. Bessell & J. M. Brett (1988) and then estimated θ_* based on the conversion. Table 6 presents the estimated source radii for the events, along with the angular Einstein radii and relative proper motions (μ) between the source and lens. The relative proper motion is calculated from the measured values of $\theta_{\rm E}$ and $t_{\rm E}$ as $\mu = \theta_{\rm E}/t_{\rm E}$.

5. Physical Parameters of Planetary Systems

The physical parameters of the lens can be constrained by the lensing observables. In a lensing event, these observables include the event timescale $t_{\rm E}$, angular Einstein radius $\theta_{\rm E}$, and microlens parallax $\pi_{\rm E}$. These quantities are related to the lens mass (M) and distance ($D_{\rm L}$) through the relations

$$t_{\rm E} = \frac{\theta_{\rm E}}{\mu}; \quad \theta_{\rm E} = \sqrt{\kappa M \pi_{\rm rel}}; \quad \pi_{\rm E} = \frac{\pi_{\rm rel}}{\theta_{\rm E}}. \tag{4}$$

Here, $\kappa = 4G/(c^2{\rm au})$, $\pi_{\rm rel} = {\rm au}(1/D_{\rm L} - 1/D_{\rm S})$, and $D_{\rm S}$ denotes the distance to the source. When all of these observables are fully measured, the lens mass and distance can be uniquely determined using the A. Gould (2000) relation

$$M = \frac{\theta_{\rm E}}{\kappa \pi_{\rm E}}; \quad D_{\rm L} = \frac{\rm au}{\pi_{\rm E}\theta_{\rm E} + \pi_{\rm S}}. \tag{5}$$

For the analyzed events, lensing observables were partially measured: the timescale was determined for all events, the angular Einstein radius was measured for all events, and no event had its microlens parallax measured. To estimate M and $D_{\rm L}$, we conduct a Bayesian analysis that integrates constraints from the measured lensing observables with priors from a Galaxy model and a mass function model for lens objects. The Galaxy model provides priors on the physical and dynamical distributions of lens objects within the Galaxy.

In the initial step of the Bayesian analysis, we generated a large set of artificial lensing events using a Monte Carlo simulation: 10^6 events were produced by disk lenses, and another 10^6 events were generated by bulge lenses. The physical parameters (M_i, $D_{{\rm L},i}$, $D_{{\rm S},i}$, μ_i) were assigned based on the prior mass function and Galaxy models. Specifically, we used the mass function model from Y. K. Jung et al. (2018) and the Galaxy model for physical and dynamical distributions from Y. K. Jung et al. (2021). We then computed the lensing observables ($t_{{\rm E},i}$, $\theta_{{\rm E},i}$) for each synthetic event using the relations in Equation (4). For each simulated event, we calculated a relative event rate by considering the density distributions of the lens and source, the transverse speed distribution between them, and weighting by the Einstein radius ($\theta_{\rm E}$) and transverse speed ($v_\perp$), as described in Equations (2.1.2) and (2.2.2) of C. Han & A. Gould (1995). The weights for $\theta_{\rm E}$ and $v_\perp$ are applied because events with larger lensing cross-sections ($\theta_{\rm E}$) and higher relative speeds have a greater probability of being lensed. In the next step, we constructed posterior distributions for the lens mass and distance by adding the rates of synthetic events lying within the ranges of the lensing observables of each event. In this stage, we assigned a weight to the event,

$$w_i = \left(-\frac{\chi_i^2}{2}\right); \qquad \chi_i^2 = \left[\frac{t_{{\rm E},i} - t_{\rm E}}{\sigma(t_{\rm E})}\right]^2 + \left[\frac{\theta_{{\rm E},i} - \theta_{\rm E}}{\sigma(\theta_{\rm E})}\right]^2, \tag{6}$$

where ($t_{\rm E}$, $\theta_{\rm E}$) represent the measured event timescale and angular Einstein radius from modeling, and [$\sigma(t_{\rm E})$, $\sigma(\theta_{\rm E})$] indicate their measurement uncertainties.

Figures 10 and 11 illustrate the posterior distributions for the masses of the planet hosts and the distances to the planetary systems. Table 7 summarizes the estimated physical parameters, including the masses of the planet hosts ($M_{\rm h}$) and planets ($M_{\rm p}$), the distance to the planetary system, and the projected separation between the planet and its host ($a_\perp$). For KMT-2022-BLG-1790 and KMT-2023-BLG-2209, the outer

Table 7
Physical Parameters of Planetary Systems

Event	Solution	M_h ($M_\odot$)	M_p (M_J)	D_L (kpc)	$a_\perp$ (au)	p_{disk} (%)	p_{bulge} (%)
KMT-2017-BLG-2197	Inner	$0.36^{+0.34}_{-0.20}$	$8.84^{+8.29}_{-4.91}$	$7.80^{+1.02}_{-1.31}$	$15.91^{+2.08}_{-2.68}$	25	75
	Outer	⋯	$6.93^{+6.50}_{-3.85}$	⋯	$6.65^{+0.87}_{-1.12}$	⋯	⋯
KMT-2022-BLG-1790	Outer	$0.58^{+0.32}_{-0.30}$	$1.73^{+0.95}_{-0.89}$	$6.48^{+0.92}_{-1.28}$	$5.25^{+0.75}_{-1.04}$	35	65
KMT-2022-BLG-2076	Inner	$0.67^{+0.35}_{-0.35}$	$0.88^{+0.46}_{-0.45}$	$5.57^{+1.25}_{-1.55}$	$5.67^{+1.28}_{-1.58}$	71	29
	Outer	⋯	$0.86^{+0.45}_{-0.44}$	⋯	$4.41^{+0.99}_{-1.23}$	⋯	⋯
KMT-2023-BLG-2209	Outer	$0.73^{+0.35}_{-0.35}$	$0.80^{+0.38}_{-0.38}$	$5.57^{+1.51}_{-1.77}$	$3.51^{+0.95}_{-1.12}$	64	36

solutions are strongly preferred over the inner solutions, with $\Delta\chi^2 = 43.9$ and 80.3, respectively. Thus, we base our parameter estimates on the outer solutions. In contrast, for KMT-2017-BLG-2197 and KMT-2022-BLG-2076, the χ^2 values of the inner and outer solutions are nearly identical. In these cases, we separately estimate the parameters for each solution. The physical parameters were estimated based on the constraints provided by the measured timescale and angular Einstein radius. In the events with severe inner–outer degeneracy, the values of t_E and θ_E are nearly identical between the inner and outer solutions. As a result, the expected posterior distributions for each solution are almost the same. The only significant difference between the inner and outer solutions is the projected planet–host separation. Therefore, the expected physical separation in each solution was determined using the relation $a_\perp = sD_L\theta_E$.

In cases of inner–outer degeneracy, the estimated planet masses for the inner and outer solutions are similar, as both solutions yield comparable planet-to-host mass ratios, though the projected separations differ. The host star of KMT-2017-BLG-2197 is an M-type dwarf, while those of KMT-2022-BLG-1790, KMT-2022-BLG-2076, and KMT-2023-BLG-2209 are K-type dwarfs. All planets are gas giants, with masses ranging from ~0.3 to ~9M_J. Also listed in Table 7 are the probabilities of the planetary systems being located in the disk (p_{disk}) or the bulge (p_{bulge}). The planetary systems KMT-2017-BLG-2197L and KMT-2022-BLG-1790L are more likely situated in the bulge, while KMT-2022-BLG-2076 and KMT-2023-BLG-2209 are more likely to be in the disk.

6. Summary and Conclusion

We analyzed data from previous years of the KMTNet survey to detect weak planetary signals in lensing events involving faint source stars. We initially identified events with potential short-term anomalies, then validated these signals by conducting detailed modeling with rereduced data. This approach resulted in the discovery of four planetary systems: KMT-2017-BLG-2197L, KMT-2022-BLG-1790L, KMT-2022-BLG-2076L, and KMT-2023-BLG-2209L.

The modeling of these events yielded two possible solutions due to the well-known inner–outer degeneracy. The degeneracy was resolved for KMT-2022-BLG-1790 and KMT-2023-BLG-2209, where photometric errors are relatively small, whereas it remains significant for the other events.

The estimated masses of the planets and their hosts are approximately (M_p/M_J, $M_h/M_\odot$) ~ (0.36, 7.9) for KMT-2017-BLG-2197L, ~(0.6, 1.7) for KMT-2022-BLG-1790L, ~(0.67, 0.9) for KMT-2022-BLG-2076L, and ~(0.73, 0.8) for KMT-2023-BLG-2209L. The planetary systems KMT-2017-BLG-2197L and KMT-2022-BLG-1790L are likely located in the Galactic bulge, while KMT-2022-BLG-2076L and KMT-2023-BLG-2209L are more likely situated in the disk.

Reporting these planets is essential for accurately estimating planet detection efficiency. Determining the distribution and frequency of planets requires a precise calculation of detection efficiency, which can be done by a comprehensive analysis of the entire sample that meets a given detection criterion. Among the planets reported in this study, two were not detected by the AnomalyFinder algorithm, despite their signals exceeding the detection threshold. Understanding the characteristics of these events could help improve the algorithm. For the three planets identified by AnomalyFinder, while each individual detection may have limited scientific significance, documenting them remains crucial. If these planets are not reported, they could be excluded from the sample used in planetary statistical analyses. Therefore, their inclusion is essential for conducting accurate demographic studies.

Acknowledgments

This research was supported by the Korea Astronomy and Space Science Institute under the R&D program (Project No. 2025-1-830-05) supervised by the Ministry of Science and ICT. This research has made use of the KMTNet system operated by the Korea Astronomy and Space Science Institute (KASI) at three host sites of CTIO in Chile, SAAO in South Africa, and SSO in Australia. Data transfer from the host site to KASI was supported by the Korea Research Environment Open NETwork (KREONET). This research was supported by KASI under the R&D program (Project No. 2024-1-832-01) supervised by the Ministry of Science and ICT. J.C.Y. and I.-G.S. acknowledge support from US NSF grant No. AST-2108414. Y.S. acknowledges support from BSF grant No. 2020740. W.Z. and H.Y. acknowledge support by the National Natural Science Foundation of China (grant No. 12133005). W.Z. acknowledges the support from the Harvard–Smithsonian Center for Astrophysics through the CfA Fellowship.

ORCID iDs

Cheongho Han https://orcid.org/0000-0002-2641-9964
Michael D. Albrow https://orcid.org/0000-0003-3316-4012
Chung-Uk Lee https://orcid.org/0000-0003-0043-3925
Yossi Shvartzvald https://orcid.org/0000-0003-1525-5041
Jennifer C. Yee https://orcid.org/0000-0001-9481-7123
Byeong-Gon Park https://orcid.org/0000-0002-6982-7722
Richard W. Pogge https://orcid.org/0000-0003-1435-3053

References

Albrow, M. 2017, MichaelDAlbrow/pyDIA: Initial release on github, v1.0.0, Zenodo, doi:10.5281/zenodo.268049
Albrow, M., Horne, K., Bramich, D. M., et al. 2009, MNRAS, 397, 2099
Bensby, T., Yee, J. C., Feltzing, S., et al. 2013, A&A, 549, A147
Bessell, M. S., & Brett, J. M. 1988, PASP, 100, 1134
Chung, S.-J., Han, C., Park, B.-G., et al. 2005, ApJ, 630, 535
Gaudi, B. S. 1998, ApJ, 506, 533
Gaudi, B. S., & Gould, A. 1997, ApJ, 486, 85
Gaudi, B. S., & Han, C. 2004, ApJ, 611, 528
Gould, A. 2000, ApJ, 542, 785
Gould, A., Han, C., Zang, W., et al. 2022, A&A, 664, A13
Gould, A., & Loeb, L. 1992, ApJ, 396, 104
Gui, Y., Zang, W., Zhai, R., et al. 2024, AJ, 168, 49
Han, C. 2006, ApJ, 638, 1080
Han, C., & Gould, A. 1995, ApJ, 447, 53
Han, C., Gould, A., Bond, I. A., et al. 2022a, A&A, 662, A70
Han, C., Gould, A., Kim, D., et al. 2022b, A&A, 663, A145
Han, C., Kim, D., Yang, H., et al. 2022c, A&A, 664, A114
Han, C., Lee, C.-U., Bond, I. A., et al. 2023a, A&A, 676, A97
Han, C., Lee, C.-U., Zang, W., et al. 2023b, A&A, 674, A90
Han, C., Udalski, A., Jung, Y. K., et al. 2024a, A&A, 685, A16
Han, C., Udalski, A., Kim, D., et al. 2021, A&A, 655, A21
Han, C., Udalski, A., Lee, C.-U., et al. 2024b, A&A, 683, A187
Herrera-Martin, A., Albrow, A., Udalski, A., et al. 2020, AJ, 159, 134
Holtzman, J. A., Watson, A. M., Baum, W. A., et al. 1998, AJ, 115, 1946
Hwang, K.-H., Choi, J.-Y., Bond, I. A., et al. 2013, ApJ, 778, 55
Hwang, K.-H., Zang, W., Gould, A., et al. 2022, AJ, 163, 43
Jung, Y. K., Han, C., Udalski, A., et al. 2021, AJ, 161, 293
Jung, Y. K., Udalski, A., Gould, A., et al. 2018, AJ, 155, 219
Jung, Y. K., Zang, W., Han, C., et al. 2022, AJ, 164, 262
Jung, Y. K., Zang, W., Wang, H., et al. 2023, AJ, 165, 226
Kervella, P., Thévenin, F., Di Folco, E., & Ségransan, D. 2004, A&A, 426, 297
Kim, D.-J., Kim, H.-W., Hwang, K.-H., et al. 2018, AJ, 155, 76
Kim, S.-L., Lee, C.-U., Park, B.-G., et al. 2016, JKAS, 49, 37
Mao, S., & Paczyński, B. 1991, ApJ, 374, 37
Nataf, D. M., Gould, A., Fouqué, P., et al. 2013, ApJ, 769, 88
Ryu, Y.-H., Udalski, A., Yee, J. C., et al. 2024, AJ, 167, 88
Shin, I.-G., Yee, J. C., Zang, W., et al. 2023, AJ, 166, 104
Shin, I.-G., Yee, J. C., Zang, W., et al. 2024, AJ, 167, 269
Wang, H., Zang, W., Zhu, W., et al. 2022, MNRAS, 510, 1778
Yang, H., Yee, J. C., Hwang, K.-H., et al. 2024, MNRAS, 528, 11
Yee, J. C., Shvartzvald, Y., Gal-Yam, A., et al. 2012, ApJ, 755, 102
Yee, J. C., Zang, W., Udalski, A., et al. 2021, AJ, 162, 180
Yoo, J., DePoy, D.L., Gal-Yam, A., et al. 2004, ApJ, 603, 139
Zang, W., Hwang, K.-H., Udalski, A., et al. 2021, AJ, 162, 163
Zang, W., Jung, Y. K., Yang, H., et al. 2023, AJ, 165, 103
Zang, W., Yang, H., Han, C., et al. 2022, MNRAS, 515, 928
Zhang, K., Gaudi, B. S., & Bloom, J. S. 2022, NatAs, 6, 782